Superconductivity and Wilson transition behaviors of lithium-rich oxides Li_mO ($m = 1$–8) under pressure based on *ab initio* calculations

Liying Song,[1] Xilian Jin,[1,*] Jisheng Li,[1] Yang Liu,[1] Lin An,[1] Yijia Chen,[1] Qingbiao Jin,[1] Tian Cui,[2,†] and Bingbing Liu[1]
[1]*State Key Laboratory of Superhard Materials, College of Physics, Jilin University, Changchun 130012, China*
[2]*Institute of High Pressure Physics, School of Physical Science and Technology, Ningbo University, Ningbo 315211, China*

(Received 12 January 2023; revised 21 July 2023; accepted 25 July 2023; published 9 August 2023)

The study of abnormal Wilson transitions from metal to nonmetal states in simple electronic systems under high pressure plays an important role in understanding the profound physical mechanisms associated with the electronic structures of materials. Moreover, such studies serve as important references for understanding complex electronic systems. Of particular interest is that Li-O systems have been demonstrated to exhibit both normal and abnormal Wilson transition behaviors at high pressure depending on the Li to O ratio, and that Li-O compounds also exhibit superconductivity. However, the pressure-induced phase transformations and superconducting properties of these materials have not been comprehensively studied, particularly for Li-rich oxides. The present work addresses this issue by conducting *ab initio* structural relaxations of Li_mO_n compounds ($m \leqslant 8$, $n \leqslant 2$) at selected pressures ranging from 1 atm to 200 GPa using density-functional theory. Accordingly, we obtain detailed structural information for all stable compounds based on their formation enthalpies with respect to decomposition into other Li-O compounds or elemental Li and O solids. The results demonstrate that the parity of m in Li-rich Li_mO compounds determines their metallization or antimetallization features under applied pressures rather than the magnitude of m. The $C2/c$ phase of Li_8O, which exhibits an antimetallization feature with increasing pressure, is found to be superconducting at a temperature of 5.54 K under an applied pressure of 100 GPa. In stark contrast to other Li-rich compounds and most hydrides whose superconductivity is primarily affected by the electron density of states at the Fermi level, the superconductivity of $C2/c$-phase Li_8O is mainly affected by an increasing average electron-phonon matrix element over the Fermi surface and a decreasing average phonon frequency with increasing pressure.

DOI: 10.1103/PhysRevB.108.054102

I. INTRODUCTION

Metal-insulator phase transitions are very important physical phenomena in the field of condensed-matter physics. Nearly all metal-insulator transitions can be grouped into two types. The first type involves phase transitions related to complex electron systems, such as Mott, Anderson, and Slater transitions, whose electronic structures cannot be described adequately by the mean-field approximation or Landau-Fermi liquid theory [1,2]. Understanding these phase transitions is of important significance for solving a number of advanced problems in condensed-matter physics, such as for determining the operative mechanism in unconventional superconductors. The second type of metal-insulator transition is related to materials with conventional electronic structures that can be reasonably described by Landau-Fermi liquid theory, such as Peierls and Wilson transitions, which can be attributed often to a clear physical mechanism based on energy-band theory. In particular, Wilson transitions can arise due to factors such as temperature and pressure, and are often applied for explaining the metal-insulator transitions occurring in compressed materials. However, metal-insulator phase transformations can rarely be attributed to single operative mechanisms in actual materials, and multiple mechanisms are often intertwined, such as is the case for VO_2 [3–6].

A great many insulator-to-metal transformations are well known to be driven by Wilson transition mechanisms in materials with simple electronic structures [7]. For example, the inducement of Wilson transitions under high pressure is an important method for synthesizing metallic hydrogen. According to the classical energy-band theory of condensed-matter physics, such Wilson transitions occur due to overlapping energy bands arising from the decreasing atomic spacing obtained under high pressure. For example, hexagonal close-packed Ar and Kr systems, which are good insulator materials at ambient pressure, undergo insulator-to-metal transitions at about 510 and 310 GPa, respectively [8,9]. Moreover, hydrogen-rich compounds have been reported to transition to metals and have high superconducting transition temperatures (T_c) under high pressure.

Nonetheless, abnormal Wilson transitions from metal to insulator or semiconductor (i.e., nonmetal) states have been observed for alkali metals and alkaline earth metals. For example, Na, Li, and Ca metals have been demonstrated to transform to nonmetal states under high pressure in a process that is sometimes referred to as pressure-induced antimetallization [10–19]. Similar phenomena have also been observed in some compounds with simple electronic structures, such

*jinxilian@jlu.edu.cn
†cuitian@jlu.edu.cn

as Li_4C [20,21]. The study of abnormal Wilson transitions in simple electronic systems plays an important role in understanding the profound physical mechanisms associated with the electronic structures of materials. Moreover, such studies serve as important references in the study of complex electronic systems, and are likely to yield relevant new physical paradigms. For example, Li-O systems have been demonstrated to exhibit both normal and abnormal Wilson transition behaviors. These behaviors have been found to be affected by the Li to O ratio, rather than the concentration of Li, which has not been reported in other materials with Wilson transitions.

We further note that a number of Li-based compounds have been reported to exhibit superconductivity at high pressures. For example, the $P6/mmm$ phase of $AsLi_7$ has a relatively high value of $T_c = 38.4$ K at 150 GPa [22]. The fcc phase of Li_3S is a metastable state found at pressures less than 640 GPa, and exhibits a high T_c of 80 K at 500 GPa [23]. The pressure-induced Li_6P electride exhibits a T_c of 39.33 K at 270 GPa [24]. Similarly, Li_5C was predicted to have a high T_c of 48.3 K at 210 GPa [25], and Li_9Te, with the highest concentration of Li_6 octahedra, is superconducting with a T_c of 10.2 K at 75 GPa [26]. Finally, $Li_{10}Se$ has been estimated to exhibit the highest T_c value of 16 K at 50 GPa, which is the lowest pressure to induce superconductivity among Li-based chalcogen electrides [27]. However, oxygen, which is one of the most abundant and important elements, can change from an insulating state to a metallic state at high pressures, and can transform into a superconducting state at low temperature [28–31]. Hence, the superconductivity of Li-O compounds has also have attracted extensive attention. Most of the known Li-O compounds, such as Li_2O, Li_2O_2, LiO_4, Li_5O_3, Li_4O_3, and Li_6O, are oxygen rich [32–39]. However, among these, only the superconducting properties of LiO_4 with a T_c up to 12.2 K at 10 GPa have been reported [39]. Moreover, the superconducting properties and pressure-induced phase transformations of Li-rich oxides have not been comprehensively studied.

The present work addresses this issue by conducting *ab initio* structural relaxations of Li_mO_n compounds ($m \leqslant 8$, $n \leqslant 2$) at selected pressures ranging from 1 atm to 200 GPa using density-functional theory (DFT), and thereby obtain detailed structural information for all stable compounds based on their formation enthalpies with respect to decomposition into other Li-O compounds or elemental Li and O solids. Lattice dynamics and electron-phonon coupling (EPC) calculations are also conducted. The results clearly demonstrate that the parity of m determines the metallization or antimetallization characteristics of Li-rich Li_mO crystals, rather than the magnitude of m. In addition, the superconductivity of Li_8O, which exhibits antimetallization behavior with increasing pressure, is found to be facilitated by an increasing average electron-phonon matrix element over the Fermi surface and a decreasing average phonon frequency with increasing pressure, rather than by an increasing electron density of states on the Fermi level, as would be expected.

II. COMPUTATIONS

Structural searches of Li-O compounds were conducted using ELOCR code [40]. The DFT calculations were conducted within the Perdew-Burke-Ernzerhof (PBE) parametrization of the generalized gradient approximation (GGA) [41], as implemented in the Vienna *Ab initio* Simulation Package (VASP) code [42]. The projected augmented-wave pseudopotential was used for both Li and O atoms, and the $1s2s$ and $2s4p$ electron configurations were adopted as valence states for Li and O, respectively. A plane-wave basis set with an energy cutoff value of 1000 eV was used for enthalpy calculations, and a Monkhorst-Pack k-mesh spacing of $2\pi \times 0.025$ Å^{-1} was adopted in this work. Then, the pseudopotentials were carefully tested by comparing the calculated lattice parameters obtained using the VASP code with the parameters listed in Table S1.

The lattice dynamics and EPC calculations were implemented in QE (QUANTUM ESPRESSO) code [43] using Trouiller-Martins–type norm-conserving pseudopotentials within the GGA correction of the PBE parametrization. Convergence testing gives the choice of kinetic energy cutoffs of 80 Ry, and the Monkhorst-Pack (MP) [44] grids of k-point sampling for each phase using a grid of spacing $2\pi \times 0.025$ Å^{-1} in the Brillouin zone (BZ) to ensure the reliability of the results. Phonon-dispersion curves were calculated using a q-mesh density of $2\pi \times 0.04$ Å^{-1} in the first BZ for the interpolation of the force constants, and phonon density of state (PHDOS) curves were calculated using a denser mesh of $2\pi \times 0.025$ Å^{-1}. Subsequently, EPC calculations were conducted in the first BZ on the same MP q-point meshes using individual EPC matrices obtained with a grid of spacing $2\pi \times 0.04$ Å^{-1}. All the convergences of the plane-wave basis set and MP sampling were carefully examined by employing higher kinetic energy cutoffs and denser grid sets.

The Fermi-surface filling parameter (FSFP) is a good means of defining the ratio of free electrons in a metallic material, and can therefore serve as a good measure of the degree of metallization. The FSFP can be obtained as follows [21]:

$$\zeta = \left(\frac{1}{N_k}\right) \sum_{kn} \delta(\varepsilon_{kn} - \varepsilon_F), \tag{1}$$

where N_k is the number of electron-momentum points used for sampling in the first BZ, the Kohn-Sham energy in electron energy band n at a given electron-momentum k is denoted as ε_{kn}, ε_F is the Fermi energy of the electron system, and $\delta(\varepsilon_{kn} - \varepsilon_F)$ is the delta function.

The Eliashberg phonon spectral function $\alpha^2F(\omega)$ can be defined as

$$\alpha^2F(\omega) = \frac{1}{2\pi N(\varepsilon_F)} \sum_{qv} \frac{\gamma_{qv}}{\omega_{qv}} \delta(\omega - \omega_{qv}), \tag{2}$$

where $N(\varepsilon_F)$ is the electron DOS at the Fermi level, ω is the phonon frequency, q and v are the wave vector and mode index, respectively, ω_{qv} is the phonon frequency, and the phonon linewidth γ_{qv} is defined as follows:

$$\gamma_{qv} = \lambda_{qv}\, \pi N(\varepsilon_F) \omega_{qv}^2. \tag{3}$$

Here, λ_{qv} is the electron-phonon coupling constant. Superimposing γ_{qv} on each mode yields the following [45]:

$$\gamma_{qv} = 2\pi\omega_{qv} \sum_{kmn} \left|g^{qv}_{k'm,kn}\right|^2 \delta(\epsilon_{k'm} - E_F)\delta(\epsilon_{kn} - E_F), \tag{4}$$

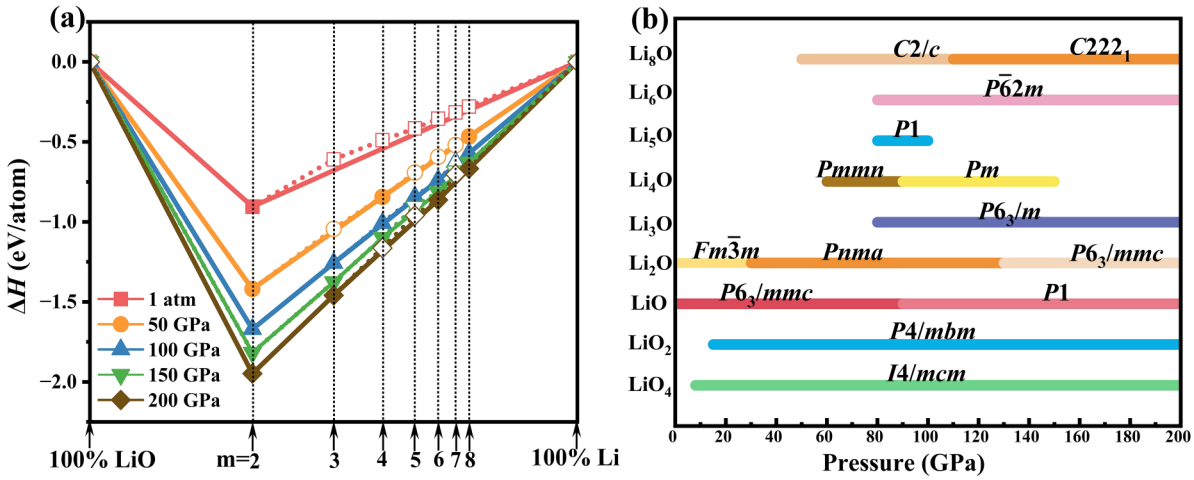

FIG. 1. (a) Stability of lithium-rich Li_mO compounds ($m = 2$–8) at different pressures based on their relative ground-state enthalpies (with respect to Li_2O_2 and Li) as a function of m. The tie lines represent convex hulls obtained by joining together globally stable structures at corresponding pressures with same marker colors. (b) Predicted pressure ranges of stability for different space groups of Li_mO_n compounds. Among them, LiO_2 and LiO_4 were reported previously [39].

where $|g^{qv}_{k'm,kn}|$ is the electron-phonon coupling matrix element and $\delta(\epsilon_{k'm} - E_F)\delta(\epsilon_{kn} - E_F)$ is the Fermi-surface nested function. This value of λ_{qv} can be applied to express the value of λ_{qv} over all q and v as follows:

$$\lambda = \sum_{qv} \lambda_{qv} = \sum_{qv} \frac{\gamma_{qv}}{\pi N(\varepsilon_F)\omega^2_{qv}}. \tag{5}$$

We can now substitute Eq. (5) within Eq. (2) to obtain $\alpha^2F(\omega)$ as follows:

$$\alpha^2F(\omega) = \frac{1}{2}\sum_{qv} \lambda_{qv}\omega_{qv}\delta(\omega - \omega_{qv}). \tag{6}$$

The present work obtains $\alpha^2F(\omega)$ by integrating ω_{qv} over the entire BZ region, as described previously [46]. Finally, the logarithmically averaged value of ω is defined as

$$\omega_{\log} = \exp\left[\frac{2}{\lambda}\int_0^\infty \frac{d\omega}{\omega}\,\alpha^2F(\omega)\ln\omega\right]. \tag{7}$$

The behavior of phonon-mediated superconductors can be described accurately by Migdal-Eliashberg theory [47]. From this perspective, the value of T_c for a superconductor can be estimated by the Allen-Dynes formula as follows [48]:

$$T_c = \frac{\omega_{\log}}{1.2}\exp\left[\frac{-1.04(1+\lambda)}{\lambda - \mu^*(1+0.62\lambda)}\right], \tag{8}$$

where μ^* is the electron Coulomb repulsion pseudopotential parameter. This approximation has been found to be highly accurate for many materials for which $\lambda < 1.5$. Then, the variation in λ can be analyzed using the rigid muffin-tin theory developed by Gaspari and Gyorffy [49]. Finally, λ can be defined by McMillan's strong coupling theory as follows:

$$\lambda = \frac{N(\varepsilon_F)\langle I^2\rangle}{M\langle\omega^2\rangle} = \eta N(\varepsilon_F), \tag{9}$$

where $\langle I^2\rangle$ is an average of the electron-phonon matrix element over the Fermi surface, M is the atomic mass, $\langle\omega^2\rangle$ is a weighted average of the square of the phonon frequency, and $\eta = \frac{\langle I^2\rangle}{M\langle\omega^2\rangle}$.

III. RESULTS AND DISCUSSION

Stable Li_mO_n compounds were determined at different pressures based on their formation enthalpies ΔH calculated per atom as follows:

$$\Delta H(Li_mO_n) = [H(Li_mO_n) - mH(Li) - nH(O)]/(m+n), \tag{10}$$

where the enthalpy values H were calculated per chemical unit for each compound. The Li_mO_n compounds obtained at different pressures are plotted as convex-hull curves in Fig. 1(a) as a function of m and in Fig. S1 in Supplemental Material (SM) [50] for different O-rich compounds. Those structures with ΔH values lying on the convex hull are considered thermodynamically stable [51]. The phase diagram obtained accordingly for the crystalline Li_mO_n systems is presented in Fig. 1(b). In addition, the detailed structural information obtained for the thermodynamically stable Li_mO_n phases is summarized in Table S1 in SM for pressures ranging from 1 atm to 200 GPa. The stable crystalline structures observed herein are consistent with the structures observed in previous experimental and theoretical studies [38–42,52–55].

The stable Li_mO_n compounds observed herein can be divided into Li-rich compounds Li_mO ($m > 1$) and Li-poor compounds LiO_n ($n > 1$). Lithium peroxide (Li_2O_2) can be viewed as a transition type of Li_mO_n compound in the continuum from Li-poor to Li-rich oxides. Our calculations redemonstrated that Li_2O_2 crystallizes into a hexagonal form with a space group of $P6_3/mmc$ at pressures less than 90 GPa [39]. The energetic favorability of the other space groups of Li_2O_2 at greater pressures can be determined according to their calculated values of H (Table S2). Recent studies have reported that the hexagonal $P6_3/mmc$ phase transforms into a monoclinic $P2_1/c$ phase at pressures greater than about 90 GPa [39,56]. However, the results obtained in the current

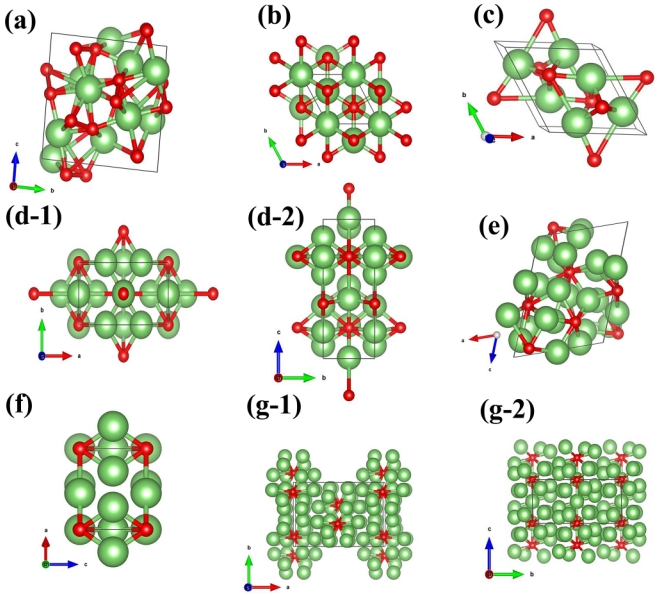

FIG. 2. Crystal structures of predicted stable Li_mO_n systems: (a) Li_2O_2 with space group $P1$; (b) Li_2O with space group $P6_3/mmc$; (c) Li_3O with space group $P6_3/m$; (d) Li_4O with space groups $Pmmn$ (d-1) and Pm (d-2); (e) Li_5O with space group $P1$; (f) Li_6O with space group $P\bar{6}2m$; and (g) Li_8O with space groups $C2/c$ (g-1) and $C222_1$ (g-2). Standard convention employed herein is that green and red spheres represent Li and O atoms, respectively.

study indicate that the $P1$ phase of Li_2O_2 is more energetically favorable than the $P2_1/c$ phase in the pressure range from 90 to 200 GPa, due to the lower enthalpy value as shown in Fig. S2(a), Table S2. The crystal structure of the predicted stable $P1$-phase Li_2O_2 system is illustrated in Fig. 2(a). We have calculated the Gibbs free energy of $P1$ and $P2_1/c$ structures of Li_2O_2 at 100 GPa. Considering the influence of temperature on the energy of the system, the results show that the enthalpy value in $P1$ structure is still lower than $P2_1/c$ structure in the temperature range of $0 \sim 1000$ K, assuming that they still do not melt within the range, as shown in Fig. S2(b). However, the enthalpy difference is quite small between the two structures, and may indicate coexistence of the phases depending on experimental conditions. The theoretical x-ray-diffraction (XRD) curves of the three space-group systems calculated with a wavelength of 1.541 Å (Fig. S3) should help to verify the observability of the $P1$ phase for Li_2O_2 at the reported pressures experimentally in the future. Moreover, the corresponding atomic structures are given as insets in the figure. Of particular interest is that equivalent XRD patterns are obtained for the $P2_1/c$ system reported herein and that reported previously [39], even though the two $P2_1/c$ structures are quite different in shape [57].

Our calculations conducted for Li_2O demonstrated that the face-centered cubic $Fm\bar{3}m$ phase and the orthorhombic $Pnma$ phase were most energetically favorable in the pressure ranges of 1 atm to 30 GPa and from 30 to 130 GPa, respectively, which is in agreement with the results of recent experimental and theoretical studies [38,39,53,55,58]. At higher pressure, Li_2O stabilizes with a hexagonal $P6_3/mmc$ lattice up to a pressure of at least 200 GPa. The crystal structure of the predicted stable $P6_3/mmc$-phase Li_2O system is illustrated in Fig. 2(b). Regarding the structure of Li_3O at ambient pressure, Wu *et al.* [59]. synthesized Li_3O in a gaseous form at ambient pressure in 1979. The $P6_3/m$ phase was obtained for Li_3O at pressures greater than or equal to about 80 GPa in the present work, and the corresponding crystal structure is illustrated in Fig. 2(c). At relatively low pressure, Li_4O is found to conform to the $Pmmn$ space group, undergoes a phase transition to the Pm space group at a pressure of 90 GPa, and can be stable up to 150 GPa. The crystal structures of the predicted stable Li_4O systems are given in Fig. 2(d) with space groups $Pmmn$ and Pm given as (d-1) and (d-2), respectively. In the pressure range from 80 to 100 GPa, Li_5O conforms to a triclinic crystal in the $P1$ space group with the crystal structure given in Fig. 2(e). According to the convex hull in Fig. 1(a), Li_7O decomposes into Li_6O and Li_8O for pressures ranging from 100 to 200 GPa. The crystal structure of the predicted stable $P\bar{6}2m$-phase Li_6O system at a pressure of 150 GPa is illustrated in Fig. 2(f). The phonon spectra of Li_2O_2 and the Li-rich Li_2O–Li_6O compounds in their stable space groups [Figs. S4(a)–S4(f)] exhibit no imaginary frequencies in the BZ, and thereby confirm the stability of their lattice dynamics. Meanwhile, the lowest-enthalpy Li_7O structure observed at a pressure of 100 GPa resides in the $Imma$ space group, and the crystal structure is illustrated in SM [Fig. S4(h)]. We can see from the convex-hull graph curve at different pressures that the enthalpy differences from the points on the curve are small. The absence of imaginary frequencies in the BZ of the phonon spectrum of Li_7O in the $Imma$ space group [Fig. S4(g)] also confirms the stability of its lattice dynamics. Considering the possibility of an energy barrier, the results suggest that Li_7O compounds may be thermodynamically metastable. The Li_8O compound is stable in the transform from the $C2/c$ phase structure to the $C222_1$ phase structure at about 110 GPa. The crystal structures of the predicted stable Li_8O systems are given in Fig. 2(g) with space groups $C2/c$ and $C222_1$ given as (g-1) and (g-2), respectively.

The mechanical properties of these materials are essential information when evaluating their structural stability. To this end, we calculated the elastic constants C_{ij} (GPa) for Li_mO_n compounds with different stable space groups at different pressures, and the results are listed in Table S3. The mechanical stability of the hexagonal phases associated with space groups $P6_3/mmc$, $P\bar{6}2m$, and $P6_3/m$ is guaranteed if the values of the five independent elastic constants C_{11}, C_{12}, C_{13}, C_{33}, and C_{31} conform to the inequalities $C_{31} > 0$, $C_{11} > |C_{12}|$, and $(C_{11} + 2C_{12})\,C_{33} > 2C_{13}^2$ [60]. As can be seen, these phases are guaranteed to be stable in the corresponding pressure intervals. Mechanical stability in the case of the orthonormal phases associated with space groups $C222_1$, $Imma$, and $Pmmn$ is guaranteed if the independent elastic constants C_{22}, C_{33}, C_{31}, C_{55}, C_{66}, C_{12}, C_{13}, and C_{23} satisfy the inequalities $C_{11} > 0$, $C_{22} > 0$, $C_{33} > 0$, $C_{11} + C_{22} + C_{33} + [2(C_{12} + C_{13} + C_{23})] > 0$, $(C_{11} + C_{22} - 2C_{13}) > 0$, $C_{31} > 0$, $C_{55} > 0$, $C_{66} > 0$, and $(C_{22} + C_{33} - 2C_{23}) > 0$ [61]. An examination of these values indicates that all these phases are mechanically stable in the corresponding pressure intervals. Finally, the mechanical stability of phases with monoclinic and triclinic crystal structures, including space groups $P1$, Pm, and $C2/c$, are guaranteed

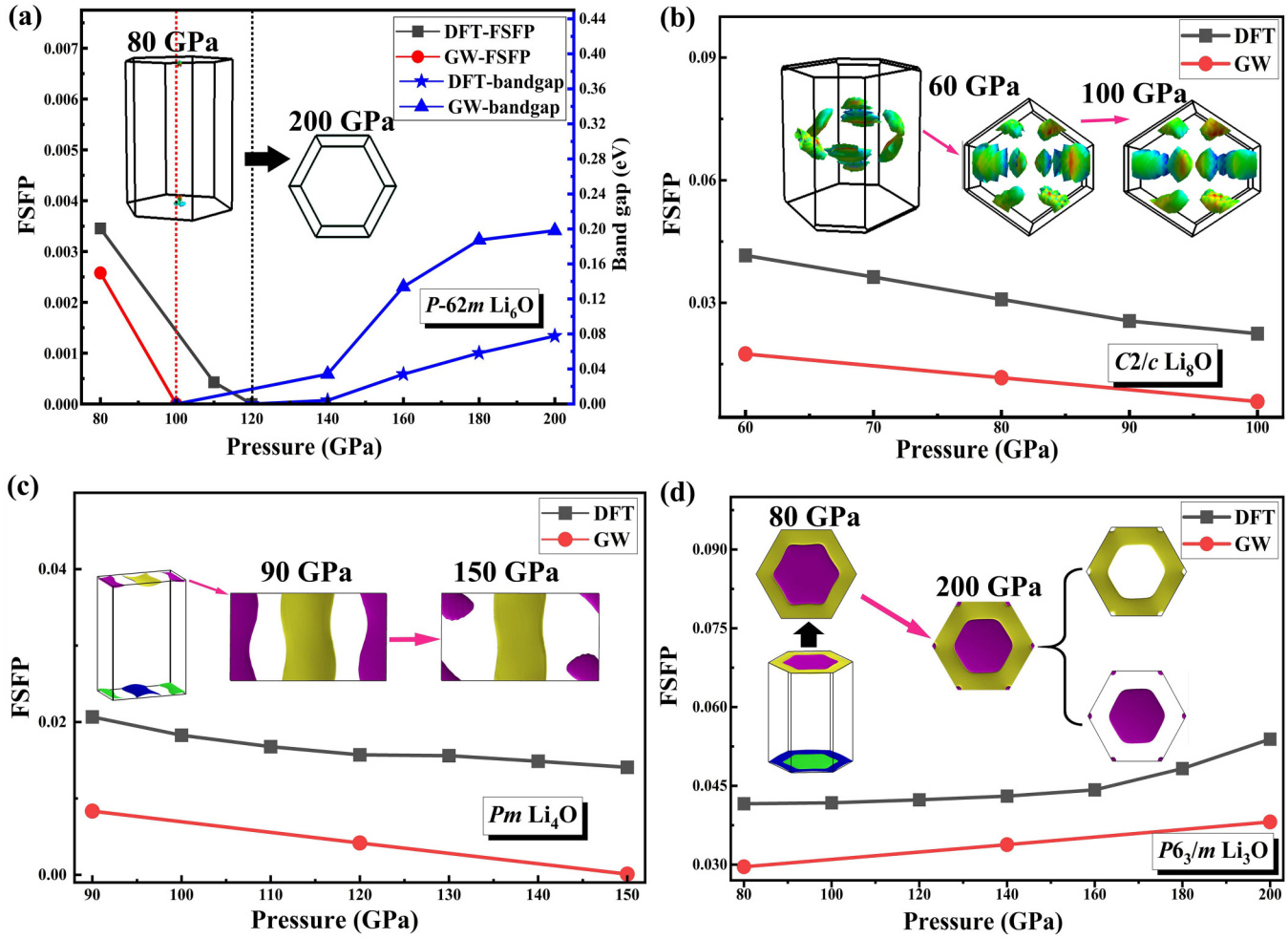

FIG. 3. Evolution of pressure-induced metallization or antimetallization behaviors in stable Li-rich oxide compounds of Li_mO ($m = 3, 4, 6, 8$) by DFT and *GW* methods. (a) FSFP and energy band gap in Li_6O; red and black dashed lines represent pressure points at which energy band gap begins to appear in *GW* method and DFT method, respectively. (b) FSFP in Li_8O; (c) FSFP in Li_4O; and (d) FSFP in Li_3O. Three-dimensional (3D) Fermi surfaces corresponding to selected pressures are also illustrated.

if their independent elastic constants satisfy the following inequalities: $C_{11} > 0$, $C_{22} > 0$, $C_{33} > 0$, $C_{31} > 0$, $C_{55} > 0$, $C_{66} > 0$, $(C_{33}C_{55} - C_{35}^2) > 0$, $(C_{31}C_{66} - C_{46}^2) > 0$, and $(C_{22} + C_{33} - 2C_{23}) > 0$ [62]. An examination of these elastic constants indicates that all these phases are mechanically stable in the corresponding pressure intervals.

The electronic properties of the Li_mO compounds under different pressures were analyzed based on their calculated electron band structures. The electron band structure obtained for Li_6O in the $P\bar{6}2m$ space group at 80 GPa [Fig. S5(a)] indicates that $P\bar{6}2m$-phase Li_6O is metallic at this pressure with several bands passing through the Fermi level. At the higher pressures of 150 and 200 GPa, $P\bar{6}2m$-phase Li_6O developed band gaps and apparently entered a nonmetallic state [Figs. S5(b) and S5(c)]. We further note that a band gap appears with increasing pressure to 120 GPa [Fig. 3(a)] according to the DFT calculations. Obviously, the $P\bar{6}2m$ phase of Li_6O transitions from a metal to an insulator under increasing pressure in this range. It is well known that the screened Coulomb interaction (*GW*) approximations can improve the prediction of the energy band gap in contrast to the standard *ab initio* DFT calculations [21]. We used *GW* method to calculate the band gap in the nonmetallic phase of Li_6O, as shown in Fig. 3(a). The results obtained by *GW* method show that the band gap appears when the pressure is higher than 100 GPa. In addition, the band gap increases with the increase of pressure, which is consistent with the variation trend of DFT calculation; see Fig. 3(a).

Subsequently, the pressure-induced antimetallization in the $P\bar{6}2m$ phase of Li_6O, the $C2/c$ phase of Li_8O, the Pm phase of Li_4O, and metallization process in the $P6_3/m$ phase of Li_3O were investigated quantitatively according to the FSFP using Eq. (1) by the DFT and *GW* methods, respectively, and the results can be found in Figs. 3(a)–3(d). We are more concerned about the variation trend of FSFP with pressure because it is the tendency that determines whether the material has a metallization or antimetallization behaviors. From Fig. 3. we can see that the two calculation methods of DFT and *GW* demonstrate a consistent tendency, and give the same physical conclusions.

As can be seen from Fig. 3(a), the FSFP of the $P\bar{6}2m$-phase Li_6O compound decreased continuously as the pressure increased from 80 to 120 GPa by DFT calculation, which clearly verifies the observed transition from a metal to an

insulator under increasing pressure demonstrated in the preceding paragraph, and further demonstrates that this process occurs gradually and monotonically with increasing pressure. Similar metal-to-nonmetal transitions have been observed with increasing pressure for some alkali metals. For example, the metallic Na-$tI19$ phase of Na has been demonstrated to transition to the insulating Na-$hP4$ phase with a highly distorted double-hexagonal close-packed structure at a pressure of about 200 GPa [16]. However, the process observed for Li_6O is quite different from that observed for Na, in that the Li_6O crystal remained in the $P\bar{6}2m$ phase throughout the metal-to-insulator transition. Obviously, the metal-to-insulator transition behavior of $P\bar{6}2m$-phase Li_6O cannot be attributed to a first-order phase transition.

Similar to that observed for $P\bar{6}2m$-phase Li_6O, the results in Fig. 3(b) indicate that the FSFP of the $C2/c$-phase Li_8O compound also decreased continuously as the pressure increased from 60 to 100 GPa, which confirms a metal-to-insulator transition process for Li_8O with increasing pressure. This effect can be further evaluated according to the calculated electron band structures obtained for Li_8O in the $C2/c$ space group at a pressure of 100 GPa [Fig. S6(a)] and in the $C222_1$ space group at 150 GPa [Fig. S6(b)]. A plot of the band-gap energy as a function of pressure [Fig. S6(d)] indicates that the band-gap energy first decreases in the $C222_1$ space group and then increases with further pressure increase. The PDOS curves of $C2/c$-phase Li_8O at different pressures of 60 GPa [Fig. S7(a)], 80 GPa [Fig. S7(b)], and 100 GPa [Fig. S7(c)] reveal hybridizations of Li_p, Li_s, and O_p electrons under pressure. Here, the metallic properties of $C2/c$-phase Li_8O are dominated by the Li_2p state electrons [Fig. S7(d)].

Anomalous Wilson transitions induced by pressure can also be observed in other Li-rich compounds with even Li ratios, such as Li_4O and Li_2O systems. As can be seen from Fig. 3(c), the FSFP of the Pm-phase Li_4O compound decreased continuously as the pressure increased from 90 to 120 GPa, indicating that the metallic properties of the compound weakened with increasing pressure. However, the impact of pressure on the FSFP became considerably reduced with further pressure increase up to 150 GPa. The calculated electron band structure and the two-dimensional (2D) electron localization function (2D-ELF) for Li_4O in the $Pmmn$ space group at a pressure of 80 GPa [Figs. S8(a) and S8(c)] confirms the insulator behavior of the material. Here, the ELF spans values ranging from 0 to 1, where an ELF of 1 suggests isolated electron pairs, an ELF of 0.5 reflects probable electron-gas–like pairs, and an ELF of 0 corresponds to nonelectron localization [63]. The obtained 2D-ELF plot indicates that the conductivity of the material derives from connected regions within the red rectangles, and nearly free electrons with an ELF value of 0.5 are confined in the interstitial positions of atoms in Pm-phase Li_4O as shown in Fig. S8(d). Meanwhile, the electron band structure of Pm-phase Li_4O [Fig. S8(b)] at a pressure of 100 GPa exhibits Van Hove singularity (VHS) points in the band diagrams near the Fermi level at high-symmetry k points from Y-A and E-C [64,65]. The electron band structures of Li_2O calculated at different pressures of 1 atm [Fig. S9(a)], 50 GPa [Fig. S9(b)], 100 GPa [Fig. S9(c)], and 200 GPa [Fig. S9(d)] demonstrate that the different phases of Li_2O are all wide-gap insulators in the pressure range considered. The antimetallization behavior in of the Li_2O system is illustrated by the continuously increasing band-gap energy with increasing pressure, which does not follow a Wilson transition.

In contrast to the other Li-O phases considered, the results in Fig. 3(d) indicate that the FSFP of the $P6_3/m$-phase Li_3O compound increased continuously with increasing pressure from 80 to 200 GPa, which represents pressure-induced metallization. The calculated electron band structures of Li_3O ($P6_3/m$ phase) at 150 GPa [Fig. S10(a)] and Li_5O ($P1$ phase) at 100 GPa [Fig. S10(b)] demonstrate that both Li_3O and Li_5O maintain their metallic properties in the pressure range considered, and several bands are observed to pass through the Fermi level. In addition, a VHS appears in the band diagram of $P6_3/m$-phase Li_3O at high-symmetry k points from A-H. Our calculations also demonstrated the occurrence of pressure-induced metallization for the metastable phase of Li_7O phase.

The results obtained herein for Li-rich Li_mO oxides demonstrated that pressure-induced antimetallization and metallization properties were, respectively, modulated according to even and odd values of m. These findings are further confirmed by the plot (Fig. S11) of the band-gap energy of Li_2O and the electron DOS of Li_mO ($m = 3$–8) at the Fermi level with respect to pressure, where spherical markers represent structures for which m is even and square markers represent structures for which m is odd. Obviously, the parity of m determines the metallization or antimetallization characteristics of Li-rich Li_mO crystals, rather than the magnitude of m.

The ELF isosurface obtained for $C2/c$-phase Li_8O [Fig. S6(c)] at a pressure of 100 GPa shows similar localized interstitial electrons to those observed for Li_9Te and $Li_{10}Se$, which are both superconducting with respective T_c values of 10.2 K at 75 GPa and 16 K at 50 GPa [26,27]. Accordingly, application of Bardeen-Cooper-Schrieffer theory [66] and the McMillan-Allen-Dynes equation [48] with a Coulomb pseudopotential of $\mu^* = 0.1$ yields a T_c value of 5.5481 K for $C2/c$-phase Li_8O at 100 GPa with an EPC parameter (λ) of 0.6175 (Table S5).

The phonon-dispersion curves obtained for $C2/c$-phase Li_8O at a pressure of 100 GPa are presented in the left panel of Fig. 4, where the extent of the red areas is in direct proportion to the intensity of electron-phonon interactions. Hence, we can conclude that the vibration modes near the high-symmetry k points of Γ and A exhibit strong EPC interactions, which contributes significantly to the value of λ. Meanwhile, the Eliashberg spectral function $\alpha^2F(\omega)$ values shown in the right panel of Fig. 4 indicate that O vibrations contribute 12.7% and Li vibrations contribute 87.3% to the total vibrations over a wide frequency range. The right panel further provides the integrated EPC value of λ. We can see that $\alpha^2F(\omega)$ contributes relatively little to λ at frequencies greater than about 13 THz because the increase in λ over this range of frequencies is small. However, $\alpha^2F(\omega)$ contributes about 75% to the value of λ in the low-frequency region below 13 THz where the acoustic branch is located. In particular, two peaks in $\alpha^2F(\omega)$ are observed at frequencies of about 3 and 7 THz, which are mainly derived from vibration modes at the high-symmetry k-points Γ and A, respectively. Here, the A_g mode of the seventh optical branch at the high-symmetry k-point Γ contributes most to λ. This mode of vibration is illustrated in

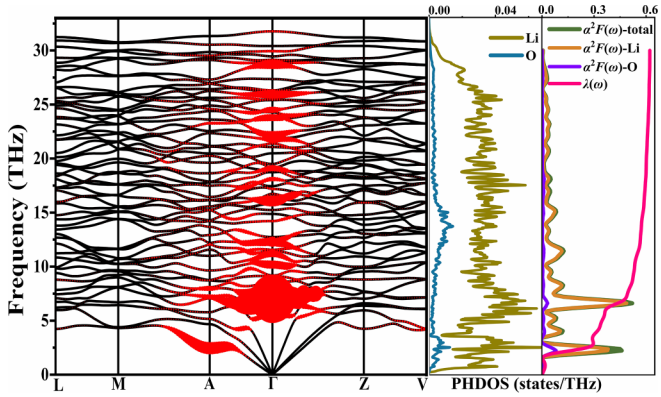

FIG. 4. Phonon properties of Li_8O in $C2/c$ space group at pressure of 100 GPa: (Left panel) calculated phonon-dispersion curves, where extent of red areas is in direct proportion to intensity of electron-phonon interactions; (center panel) phonon density of states (PHDOS) of Li and O atoms; (right panel) Eliashberg spectral function $\alpha^2F(\omega)$ values and integrated EPC value of λ.

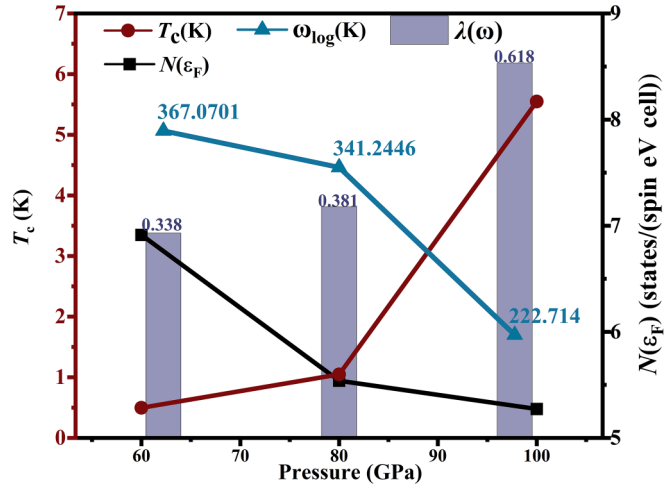

FIG. 5. Pressure dependencies of $C2/c$-phase Li_8O for critical temperature T_c (K) of superconductivity, electron-phonon coupling parameter λ, logarithmic average phonon frequency ω_{log}, and electron density of states at Fermi level $N(\varepsilon_F)$.

Fig. S12(a) for the 16 Li atoms occupying 16 kinds of $1a$ symmetric positions, and 2 O atoms occupying 2 kinds of $1a$ symmetric positions in the primitive cell of Li_8O, as shown in Table S4. We can see those adjacent atoms, such as Li1 and Li2, are associated with vibration vectors of the same magnitude, and pairs of atoms with the same color vectors represent vibrations in opposite directions. In contrast, Fig. S12(b) shows an identical A_g mode of the 22nd branch at the high-symmetry k-point Γ, which corresponds to the peak in the PHDOS of Li atoms in the middle panel of Fig. 4 at around 18 THz. The slightly weaker vibration intensity and the higher frequency of this vibration mode means that it contributes less to λ than the vibrational mode of the seventh branch. Finally, we note that the low-frequency vibrational feature of the first acoustic vibration mode at the high-symmetry k-point A illustrated in Fig. S12(c) contributes significantly to λ.

The pressure dependencies of T_c, λ, ω_{log}, and $N(\varepsilon_F)$ for $C2/c$-phase Li_8O (Table S5) are presented graphically in Fig. 5. As can be seen, T_c increases from 0.4981 K at 60 GPa to 5.5482 K at 100 GPa. This increase in T_c with increasing pressure is in sharp contrast to the pressure-dependent behavior of T_c for a Li-poor compound LiO_4, which decreases with increasing pressure [39]. In addition, we note that λ also increases with increasing pressure, which can be expected to contribute to the increasing value of T_c. However, ω_{log} and $N(\varepsilon_F)$ both decrease with increasing pressure. According to Bardeen-Cooper-Schrieffer theory [67], the value of λ should increase with increasing $N(\varepsilon_F)$, which ultimately increases the value of T_c. Therefore, the Li-rich Li_8O material violates this expectation because $N(\varepsilon_F)$ decreases and T_c increases with increasing pressure. In other words, the reduction in $N(\varepsilon_F)$ in the antimetallized compound does not negatively affect its superconductivity. This behavior also differs from the behaviors of other superconducting compounds, such as the hydrides of SH_3 and SeH_3, where a large hydrogen-dominated $N(\varepsilon_F)$ is reported to generate a strong λ and high T_c [7].

The above-discussed irregularity in the superconductivity of the $C2/c$ phase of Li_8O can be analyzed based on the average electron-phonon matrix element $\langle I^2\rangle$ over the Fermi surface and the average phonon frequency $\langle\omega^2\rangle^{1/2}$ calculated at select pressures (Table S5). Obviously, the increase in $\langle I^2\rangle$ and decrease in $\langle\omega^2\rangle^{1/2}$ dominate the upward tendency in λ with increasing pressure, which is responsible for the observed increase in T_c. Accordingly, we can conclude that the superconductivity of $C2/c$-phase Li_8O, which exhibits antimetallization behavior with increasing pressure, is facilitated by an increasing $\langle I^2\rangle$ and decreasing $\langle\omega^2\rangle^{1/2}$ with increasing pressure, rather than an increasing $N(\varepsilon_F)$, as would be expected. On the basis of what has been discussed above, $\langle I^2\rangle$ and $\langle\omega^2\rangle^{1/2}$ are mainly related to the vibration modes of Li atoms. In addition, the other metallic phases of Li-rich oxides, such as Li_3O, Li_4O, Li_5O, and Li_6O, have values of T_c tending toward zero.

IV. CONCLUSION

The present work addressed our current poor understanding of the pressure-induced phase transformations and superconducting properties of Li-rich oxides by conducting an extensive and systematic analysis of the stable crystal phases of Li_mO_n compounds ($m \leqslant 8$, $n \leqslant 2$) under ambient- and high pressures with first-principles calculations. In contrast to previous research, the $P1$ phase of Li_2O_2 has lower enthalpy values than the previously reported $P2_1/c$ phase at pressures below 200 GPa. However, the enthalpy difference is quite small between the two structures, and may indicate coexistence of the phases depending on experimental conditions. Of particular importance, our results demonstrate that the parity of m in Li-rich Li_mO compounds determines their metallization or antimetallization features under applied pressures rather than the magnitude of m. Specifically, even values of m result in pressure-induced antimetallization behavior, while odd values of m result in pressure-induced metallization. We further determined that the value of T_c observed for $C2/c$-Li_8O increased from 0.4981 K at a pressure of 60 GPa to 5.5482 K at 100 GPa. However, in sharp contrast to the behaviors of other types of Li-rich compounds and most hydrides, the value of $N(\varepsilon_F)$ observed for this material decreased with

increasing pressure owing to its corresponding antimetallization behavior. Therefore, the reduction in the electron DOS at the Fermi surface in the antimetallized Li_8O compound does not negatively affect its superconductivity. In fact, the results demonstrated that the superconductivity of Li_8O is determined by $\langle I^2 \rangle$ and $\langle \omega^2 \rangle^{1/2}$.

ACKNOWLEDGMENTS

This work was supported by the National Key R&D Program of China (Grant No. 2018YFA0305900), National Natural Science Foundation of China (Grants No. 11774119, No. 12264038, No. 51632002, No. 51572108, No. 91745203, No. 11634004, and No. 11174102), National Key Research and Development Program of China (Grant No. 2016YFB0201204), Natural Science Foundation of Inner Mongolia (Grant No. 2022MS01013), and Program for Changjiang Scholars and Innovative Research Team in University, China (Grant No. IRT15R23). Some of the calculations were conducted at the High Performance Computing Center (HPCC) of Jilin University.

[1] N. F. Mott, The basis of the electron theory of metals, with special reference to the transition metals, Proc. Phys. Soc. London, Sect. A **62**, 416 (1949).

[2] F. Evers and A. D. Mirlin, Anderson transitions, Rev. Mod. Phys. **80**, 1355 (2008).

[3] J. D. Budai, J. Hong, M. E. Manley, E. D. Specht, C. W. Li, J. Z. Tischler, D. L. Abernathy, A. H. Said, B. M. Leu, L. A. Boatner, R. J. McQueeney, and O. Delaire, Metallization of vanadium dioxide driven by large phonon entropy, Nature (London) **515**, 535 (2014).

[4] H. Zheng and L. K. Wagner, Computation of the Correlated Metal-Insulator Transition in Vanadium Dioxide from First Principles, Phys. Rev. Lett. **114**, 176401 (2015).

[5] S. Lee, K. Hippalgaonkar, F. Yang, J. Hong, C. Ko, J. Suh, K. Liu, K. Wang, J. J. Urban, X. Zhang, C. Dames, S. A. Hartnoll, O. Delaire, and J. Wu, Computation of the correlated metal-insulator transition in vanadium dioxide from first principles, Science **355**, 371 (2017).

[6] C. Weber, D. D. ORegan, N. D. M. Hine, M. C. Payne, G. Kotliar, and P. B. Littlewood, Vanadium Dioxide: A Peierls-Mott Insulator Stable Against Disorder, Phys. Rev. Lett. **108**, 256402 (2012).

[7] Q. Zhuang, X. Jin, T. Cui, D. Zhang, Y. Li, X. Li, K. Bao and B. Liu, Effect of electrons scattered by optical phonons on superconductivity in MH_3 (M = S, Ti, V, Se), Phys. Rev. B **98**, 024514 (2018).

[8] A. K. McMahan, Structural transitions and metallization in compressed solid argon, Phys. Rev. B **33**, 5344 (1986).

[9] I. Kwon, L. A. Collins, J. D. Kress, and N. Troullier, First-principles study of solid Ar and Kr under high compression, Phys. Rev. B **52**, 15165 (1995).

[10] J. B. Neaton and N. W. Ashcroft, Pairing in dense lithium, Nature (London) **400**, 141 (1999).

[11] M. Hanfland, K. Syassen, N. E. Christensen, and D. L. Novikov, New high-pressure phases of lithium, Nature (London) **408**, 174 (2000).

[12] T. Matsuoka and K. Shimizu, Direct observation of a pressure-induced metal-to-semiconductor transition in lithium, Nature (London) **458**, 186 (2009).

[13] Y. Yao, J. S. Tse, and D. D. Klug, Structures of Insulating Phases of Dense Lithium, Phys. Rev. Lett. **102**, 115503 (2009).

[14] A. Kulkarni, K. Doll, D. L. V. K. Prasad, J. C. Schon, and M. Jansen, Alternative structure predicted for lithium at ambient pressure, Phys. Rev. B **84**, 172101 (2011).

[15] J. Lv, Y. Wang, L. Zhu, and Y. Ma, Predicted Novel High-Pressure Phases of Lithium, Phys. Rev. Lett. **106**, 015503 (2011).

[16] Y. Ma, M. Eremets, A. R. Oganov, Y. Xie, I. Trojan, S. Medvedev, A. O. Lyakhov, M. Valle, and V. Prakapenka, Transparent dense sodium, Nature (London) **458**, 182 (2009).

[17] J. B. Neaton and N. W. Ashcroft, On the Constitution of Sodium at Higher Densities, Phys. Rev. Lett. **86**, 2830 (2001).

[18] K. J. Dunn and F. P. Bundy, Electrical-resistance behavior of Ca at high pressures and low temperatures, Phys. Rev. B **24**, 1643 (1981).

[19] R. A. Stager and H. G. Drickamer, Effect of temperature and pressure on the electrical resistance of four alkaline earth metals, Phys. Rev. **131**, 2524 (1963).

[20] H. Tang, B. Wan, B. Gao, Y. Muraba, Q. Qin, B. Yan, P. Chen, Q. Hu, D. Zhang, L. Wu, M. Wang, H. Xiao, H. Gou, F. Gao, H. Mao, and H. Hosono, Metal-to-Semiconductor transition and electronic dimensionality reduction of Ca_2N electride under pressure, Adv. Sci. **5**, 1800666 (2018).

[21] X. Jin, X. J. Chen, T. Cui, H. K. Mao, H. Zhang, Q. Zhuang, K. Bao, D. Zhou, B. Liu, Q. Zhou, and Z. He, Crossover from metal to insulator in dense lithium-rich compound CLi_4, Proc. Natl. Acad. Sci. USA **113**, 2366 (2016).

[22] Z. Wan, W. Xu, T. Yang, and R. Zhang, As-Li electrides under high pressure: Superconductivity, plastic, and superionic states, Phys. Rev. B **106**, L060506 (2022).

[23] C. Kokail, C. Heil, and L. Boeri, Search for high-T_c conventional superconductivity at megabar pressures in the lithium-sulfur system, Phys. Rev. B **94**, 060502(R) (2016).

[24] Z. Zhao, S. Zhang, T. Yu, H. Xu, A. Bergara, and G. Yang, Predicted Pressure-Induced Superconducting Transition in Electride Li_6P, Phys. Rev. Lett. **122**, 097002 (2019).

[25] Z. S. Pereira, G. M. Faccin, and E. Z. da Silva, Predicted superconductivity in the electride Li_5C, J. Phys. Chem. C **125**, 8899 (2021).

[26] X. Zhang, F. Li, A. Bergara, and G. Yang, Pressure-induced superconductivity in Li-Te electrides, Phys. Rev. B **104**, 134505 (2021).

[27] X. Zhang, Y. Zhao, A. Bergara, and G. Yang, Superconducting $Li_{10}Se$ electride under pressure, J. Chem. Phys. **156**, 194112 (2022).

[28] H. Fujihisa, Y. Akahama, H. Kawamura, Y. Ohishi, O. Shimomura, H. Yamawaki, M. Sakashita, Y. Gotoh, S. Takeya, and K. Honda, O_8 Cluster Structure of the Epsilon Phase of Solid Oxygen, Phys. Rev. Lett. **97**, 085503 (2006).

[29] L. F. Lundegaard, G. Weck, M. I. Mcmahon, S. Desgreniers, and P. Loubeyre, Observation of an O_8 molecular lattice in the ϵ phase of solid oxygen, Nature (London) **443**, 201 (2006).

[30] Y. Meng, P. J. Eng, J. S. Tse, D. M. Shaw, M. Y. Hu, J. Shu, S. A. Gramsch, C. Kao, R. J. Hemley, and H. K. Mao, Inelastic x-ray scattering of dense solid oxygen: Evidence for intermolecular bonding, Proc. Natl. Acad. Sci. USA **105**, 11640 (2008).

[31] K. Shimizu, K. Suhara, M. Ikumo, M. I. Eremets, and K. Amaya, Superconductivity in oxygen, Nature (London) **393**, 767 (1998).

[32] L. Andrews, Infrared spectrum, structure, vibrational potential function, and bonding in the lithium superoxide molecule LiO_2, J. Chem. Phys. **50**, 4288 (1969).

[33] V. S. Bryantsev, M. Blanco, and F. Faglioni, Stability of lithium superoxide LiO_2 in the gas phase: Computational study of dimerization and disproportionation reactions, J. Phys. Chem. A **114**, 8165 (2010).

[34] J. B. Yang, D. Y. Zhai, H. H. Wang, K. C. Lau, J. A. Schlueter, P. Du, D. J. Myers, Y. K. Sun, L. A. Curtiss, and K. Amine, Evidence for lithium superoxide-like species in the discharge product of a LiO_2 battery, Phys. Chem. Chem. Phys. **15**, 3764 (2013).

[35] J. Lu, Y. J. Lee, X. Y. Luo, K. C. Lau, M. Asadi, H.-H. Wang, S. Brombosz, J. G. Wen, D. Y. Zhai, Z. H. Chen, D. J. Miller, Y. S. Jeong, J.-B. Park, Z. Z. Fang, B. Kumar, A. Salehi-Khojin, Y.-K. Sun, L. A. Curtiss, and K. Amine, A lithium-oxygen battery based on lithium superoxide, Nature (London) **529**, 377 (2016).

[36] S. Y. Kang, Y. Mo, S. P. Ong, and G. Ceder, A facile mechanism for recharging Li_2O_2 in Li-O_2 batteries, Chem. Mater. **25**, 3328 (2013).

[37] M. M. Islam and T. Bredow, Density functional theory study for the stability and ionic conductivity of Li_2O surfaces, J. Phys. Chem. C **113**, 672 (2009).

[38] G. Yang, Y. Wang, and Y. Ma, A stable, magnetic, and metallic Li_3O_4 compound as a discharge product in a Li-air battery, J. Phys. Chem. Lett. **5**, 2516 (2014).

[39] X. Dong, J. Hou, J. Kong, H. Cui, Y. L. Li, A. R. Oganov, K. Li, H. Zheng, X. F. Zhou, and H. T. Wang, Predicted lithium oxide compounds and superconducting low-pressure LiO_4, Phys. Rev. B **100**, 144104 (2019).

[40] A code for crystal structural prediction and analysis is based on evolutional local random computational method, and is developed by our group.

[41] J. P. Perdew, K. Burke, and M. Ernzerhof, Generalized Gradient Approximation Made Simple, Phys. Rev. Lett. **77**, 3865 (1996).

[42] G. Kresse and J. Furthmuller, Efficient iterative schemes for ab initio total-energy calculations using a plane-wave basis set, Phys. Rev. B **54**, 11169 (1996).

[43] P. Giannozzi, S. Baroni, N. Bonini, M. Calandra, R. Car, C. Cavazzoni, D. Ceresoli, G. L. Chiarotti, M. Cococcioni, I. Dabo, A. D. Corso, S. D. Gironcoli, S. Fabris, G. Fratesi, R. Gebauer, U. Gerstmann, C. Gougoussis, A. Kokalj, M. Lazzeri, L. Martin-Samos, N. Marzari, F. Mauri, R. Mazzarello, S. Paolini, A. Pasquarello, L. Paulatto, C. Sbraccia, S. Scandolo, G. Sclauzero, A. P. Seitsonen, A. Smogunov, P. Umari, and R. M. Wentzcovitch, QUANTUM ESPRESSO: A modular and open-source software project for quantum simulations of materials, J. Phys.: Condens. Matter **21**, 395502 (2009).

[44] H. J. Monkhorst and J. D. Pack, Special points for Brillouin-zone integrations, Phys. Rev. B **13**, 5188 (1976).

[45] F. Rittweger, N. F. Hinsche, and I. Mertig, Phonon limited electronic transport in Pb, J. Phys.: Condens. Matter **29**, 355501 (2017).

[46] P. B. Allen, Neutron spectroscopy of superconductors, Phys. Rev. B **6**, 2577 (1972).

[47] A. B. Migdal, Interaction between electrons and lattice vibrations in a normal metal, J. Exptl. Theoret. Phys. (USSR) **34**, 1438 (1958).

[48] P. B. Allen and R. Dynes, Transition temperature of strong-coupled superconductors reanalyzed, Phys. Rev. B **12**, 905 (1975).

[49] G. Gaspari and B. Gyorffy, Electron-Phonon Interactions, *D* Resonances, and Superconductivity in Transition Metals, Phys. Rev. Lett. **28**, 801 (1972).

[50] See Supplemental Material at http://link.aps.org/supplemental/10.1103/PhysRevB.108.054102 for computational details, phonon spectra, ELF isosurfaces, electronic band structures and density of states, phonon spectra and EPC parameter of Li8O at different pressures, and structural information.

[51] S. Yang, Q. Zhuang, X. Jin, L. Song, L. Zhang, T. Cui, and B. Liu, Evolution of hydrogen dissolution and superconductivity in Re-based solid solutions under pressure studied by ab initio calculations, Phys. Rev. B **103**, 174520 (2021).

[52] L. G. Cota and P. de la Mora, On the structure of lithium peroxide, Li_2O_2, Acta Crystallogr. Sect. B: Struct. Sci., Cryst. Eng. Mater. B **61**, 133 (2005).

[53] M. D. Radin, J. F. Rodriguez, F. Tian, and D. J. Siegel, Lithium peroxide surfaces are metallic, while lithium oxide surfaces are not, J. Am. Chem. Soc. **134**, 1093 (2012).

[54] H. Foppl, Die kristallstrukturen der alkaliperoxyde, Z. Anorg. Allg. Chem. **291**, 12 (1957).

[55] D. Taylor, Thermal expansion data. II: Binary oxides with the fluorite and rutile structures, MO_2, and the antifluorite structure, M_2O, Trans. J. British Ceramic Soc. **83**, 32 (1984).

[56] N. H. Deng, W. Y. Wang, G. C. Yang, and Y. Q. Qiu, Structural and electronic properties of alkali metal peroxides at high pressures, RSC Adv. **5**, 104337 (2015).

[57] We note that the values of H calculated at a pressure of 100 GPa for the $P2_1/c$ system reported herein and that reported previously were $-2478.414\ 11$ and $-2478.412\ 69$, respectively. Accordingly, the calculated enthalpy difference between the two $P2_1/c$ configurations is $0.001\ 42/8 = 0.000\ 1775$ eV/atom. Accordingly, there are two possible configurations of $P2_1/c$-Li_2O_2 at 100 GPa; see Supplemental Material [50].

[58] T. W. D. Farley, W. Hayes, S. Hull, M. T. Hutchings, and M. Vrtis, Investigation of thermally induced Li+ ion disorder in Li_2O using neutron diffraction, J. Phys.: Condens. Matter **3**, 4761 (1991).

[59] C. H. Wu, H. Kudoa, and H. R. Ihle, Thermochemical properties of gaseous Li_3O and Li_2O_2, J. Chem. Phys. **70**, 1815 (1979).

[60] Y. Li, X. Jin, T. Cui, Q. Zhuang, Q. Lv, G. Wu, X. Meng, K. Bao, B. Liu, and Q. Zhou, Structural stability and electronic property in K_2S under pressure, RSC Adv. **7**, 7424 (2017).

[61] S. Wei, D. Li, Y. Lv, Z. Liu, C. Xu, F. Tian, D. Duan, B. Liu, and T. Cui, Ground state structures of tantalum tetraboride and triboride: An ab initio study, Phys. Chem. Chem. Phys. **18**, 18074 (2016).

[62] Z. J. Wu, E. J. Zhao, H. P. Xiang, X. F. Hao, X. J. Liu, and J. Meng, Crystal structures and elastic properties of superhard IrN_2 and IrN_3 from first principles, Phys. Rev. B **76**, 054115 (2007).

[63] Q. Zhuang, X. Jin, T. Cui, Y. Ma, Q. Lv, Y. Li, H. Zhang, X. Meng, and K. Bao, Pressure-stabilized superconductive ionic tantalum hydrides, Inorg. Chem. **56**, 3901 (2017).

[64] L. Van Hove, The occurrence of singularities in the elastic frequency distribution of a crystal, Phys. Rev. **89**, 1189 (1953).

[65] D. Fang, X. Shi, Z. Du, P. Richard, H. Yang, X. X. Wu, P. Zhang, T. Qian, X. Ding, Z. Wang, T. K. Kim, M. Hoesch, A. Wang, X. Chen, J. Hu, H. Ding, and H. H. Wen, Observation of a Van Hove singularity and implication for strong-coupling induced Cooper pairing in KFe_2As_2, Phys. Rev. B **92**, 144513 (2015).

[66] J. Bardeen, L. N. Cooper, and J. R. Schrieffer, Theory of superconductivity, Phys. Rev. **108**, 1175 (1957).

[67] J. Bardeen, L. N. Cooper, and J. R. Schrieffer, Microscopic theory of superconductivity, Phys. Rev. **106**, 162 (1957).